Single-beam multimode fiber imaging system using digital micro-mirror device and transmission matrix analysis

LIANG DENG,[1,2] JOSEPH YAN,[1] DANIEL ELSON,[3] AND LEI SU[2,*]

[1]*Department of Electrical Engineering & Electronics, University of Liverpool, Liverpool L69 3BX, UK*
[2]*School of Engineering and Materials Science, Queen Mary University of London, London E1 4NS, UK*
[3]*Department of Surgery and Cancer, Imperial College London, London SW7 2AZ, UK*
l.su@qmul.ac.uk

Abstract: This work demonstrates experimental approaches to characterize a single multimode fiber without a reference beam. Spatial light modulation is performed with a digital micro-mirror device that enables high-speed binary amplitude modulation. Intensity-only images are recorded by the camera and processed by a Bayesian inference based algorithm to retrieve the phase of output optical field as well as the transmission matrix of the fiber. The calculated transmission matrix is validated by three standards: prediction accuracy, transmission imaging, and focus generation. Also, it is found that information on mode count and eigenchannels can be extracted from the transmission matrix by singular value decomposition. This paves the way for a much more compact and cheaper single multimode fiber imaging system for many demanding imaging tasks.

OCIS codes: (060.2270) Fiber characterization; (060.2350) Fiber optics imaging; (100.5070) Phase retrieval

References and links

1. D. Psaltis and C. Moser, "Imaging with multimode fibers," Opt. Photonics News **27**(1), 24-31 (2016).
2. S. M. Popoff, G. Lerosey, R. Carminati, M. Fink, A. C. Boccara and S. Gigan, "Measuring the transmission matrix in optics: An approach to the study and control of light propagation in disordered media," Phys. Rev. Lett. **104**, 100601 (2010).
3. S. Popoff, G. Lerosey, M. Fink, A. C. Boccara and S. Gigan, "Image transmission through an opaque material," Nat. Commun. **1**, 81 (2010)
4. Y. Choi, C. Yoon, M. Kim, T. D. Yang, C. Fang-Yen, R. R. Darasi, K. J. Lee and W. Choi, "Scanner-Free and Wide-Field Endoscopic Imaging by Using a Single Multimode Optical Fiber," Phys. Rev. Lett. **109**, 203901 (2012).
5. I. N. Papadopoulos, S. Farahi, C. Moser and D. Psaltis, "Focusing and scanning light through a multimode optical fiber using digital phase conjugation," Opt. Express **20**(10), 10583-10590 (2012).
6. I. N. Papadopoulos, S. Farahi, C. Moser and D. Psaltis, "High-resolution, lensless endoscope based on digital scanning through a multimode optical fiber," Biomed. Opt. Express **4**(2), 260-270 (2013).
7. D. Loterie, S. Farahi, I. Papadopoulos, A. Goy, D. Psaltis and C. Moser, "Digital confocal microscopy through a multimode fiber," Opt. Express **23**(18), 23845-23858 (2015).
8. D. Loterie, S. A. Goorden, D. Psaltis and C. Moser, "Confocal microscopy through a multimode fiber using optical correlation," Opt. Lett. **40**(24), 5754-5757 (2015).
9. D. Kim, J. Moon, M. Kim, T. D. Yang, J. Kim, E. Chung and W. Choi, "Toward a miniature endomicroscope: pixelation-free and diffraction-limited imaging through a fiber bundle," Opt. Lett. **39**, 1921-1924 (2014).
10. A. M. Caravaca-Aguirre and R. Piestun, "Single multimode fiber endoscope," Opt. Express **25**(3), 1656-1665 (2017).
11. D. Loterie, D. Psaltis and C. Moser, "Bend translation in multimode fiber imaging," Opt. Express **25**(6), 6263-6273 (2017).
12. S. Farahi, D. Ziegler, I. N. Papadopoulos, D. Psaltis and C. Moser, "Dynamic bending compensation while focusing through a multimode fiber," Opt. Express **21**(19), 22504-22514 (2013).
13. M. Ploschner, T. Tyc and T. Cizmar, "Seeing through chaos in multimode fibres," Nat. Photon. **9**, 529-535 (2015).
14. A. M. Caravaca-Aguirre, E. Niv, D. B. Conkey and R. Piestun, "Real-time resilient focusing through a bending multimode fiber" Opt. Express **21**(10), 12881-12887 (2013).
15. A. Dremeau and F. Krakala, "Phase recovery from a Bayesian point of view: the variational approach," in Proceedings of *IEEE Trans. Acoust Speech Signal Process.* (2015).

16. S. Rosen, D. Gilboa, O. Katz and Y. Silberberg, "Focusing and Scanning through Flexible Multimode Fibers without Access to the Distal End," arXiv:1506.08586 (2015).
17. C. Yoon, Y. Choi, M. Kim, J. Moon, D. Kim and W. Choi, "Experimental measurement of the number of modes for a multimode optical fiber," Optics Letters **37**(21), 4558-4560 (2012).
18. M. Kim, Y. Choi and C. Yoon, "Maximal energy transport through disordered media with the implementation of transmission eigenchannels," Nature Photonics **6**(9), 581-585 (2012).

1. Introduction

Recently, optical multimode fiber (MMF) has become a promising candidate for endoscopic imaging due to the great number of spatial modes travelling within a small cross-section down to tens of micrometers [1]. Typically, wave propagating in MMFs suffers from mode coupling and mode dispersion and generates complex speckle patterns, which imposes a fundamental challenge for a single MMF to be used imaging applications. Although how optical fiber modes propagate in a MMF varies significantly from fiber to fiber, which scrambles the transmitted image information, the process is actually deterministic. With appropriate characterizations, MMFs can work similarly as conventional transparent imaging components such as optical lenses.

Over the past few years, the wavefront shaping technology has been investigated extensively to characterize MMFs so that a single MMF can be used to transmitted images. Light propagation in a linear medium is a linear process and can, therefore, be described by its transmission matrix (TM) [2,3], which is calculated from a set of system's input-output pairs. In Ref. [4], Choi *et al.* used a scanning mirror to modulate the input fields and obtained the output fields with off-axis holography. All the data was processed to construct the TM, leading to imaging with diffraction-limited resolution. However, this method necessitates the recording of input fields, which is time-consuming and lowers experiment operability. Compared with the scanning mirror, by offering phase-only modulations, spatial light modulator (SLM) is more widely used in wavefront shaping. Using an SLM, Papadopoulos *et al*. demonstrated focus generation [5] and point scanning based fluorescence imaging [6] with digital phase conjugation. Loterie and co-workers utilized an SLM to measure the TM of the MMF and further achieved high imaging with digital confocal [7] and optical confocal setup [8]. The importance of monitoring system stability and phase drifting is stressed in their works, as phase correction is essential for TM effectiveness. Digital micromirror device (DMD) has been used as a cheap and high-speed alternative of SLM. The rotation of micro-mirrors on board can realize binary amplitude modulation, which can also be used to measure fiber TM and to perform point-scanning imaging [9]. The previously mentioned approaches all require a reference beam, either co-propagating in the fiber [2,3] or in an external form [4-9]. However, to extract the full information of the optical field by phase-shifted or off-axis holography is at the cost of a complicated system and suffers from instability issues arising from the holographic interference process for phase retrieval.

Since the mode coupling is highly subject to the change of fiber shapes, and movements, flexible single MMF imaging is a real challenge. Normally, multimode fiber imaging systems have very limited flexibility. And it has been demonstrated that graded-index MMF [10] and high-NA MMF [11] suffer less from fiber deformations for image transmission. To improve this, Farahi *et al*. proposed a dynamic bending compensation system with the help of another single mode fiber and a virtual beacon source [12]. But the possible change to the MMF shape is carefully limited in their setup and sufficient pre-acquired data is needed to perform the re-focusing. Moreover, recent developments in theoretical models enable the prediction of fiber output after deformation [13]. To match the experimental results with the theory, the model has to be extremely accurate. Since the errors are accumulated with the increase of the image transmission distance, this method is only validated for short fibers (no more than 300 mm). Another related difficulty is that the shape of the fiber needs to be completely confirmed to model the propagation, which is hard in real applications, as the fiber will be randomly shaped. To deal with truly free deformation, A. M. Caravaca-Aguirre *et al*. demonstrated a real-time

re-focusing system based on feedback and wavefront control [14]. They used in-line interference to extract transmission matrix by dividing each input field into reference part and controlled part. This approach does not need any knowledge of fiber deformation and can obtain TM in tens of milliseconds with the help of FPGA. But the instability problem due to interference still exists as in Ref [2,3].

In this paper, we demonstrate the acquisition of the complete TM of a MMF using DMD without using interference. It involves an advanced phase retrieval algorithm [15] and therefore leads to a simplified and robust optical setup. A sufficiently large number of output fields can be measured quickly thanks to the high speed of DMD. The algorithm itself runs in a parallel way such that distributed computations can be done to accelerate the data acquisition. The calculated TM is then verified using the following three approaches. Firstly, predicted outputs for random inputs are compared with corresponding actual outputs for prediction accuracy estimation. Secondly, imaging in the transmission mode is demonstrated with pre-defined patterns. Lastly, a set of focuses is generated on the distal fiber end with the information in TM as a focus-scanning process. In addition, it has been demonstrated that one can obtain accurate mode count and eigenchannels for better energy delivery by performing singular value decomposition for transmission matrix.

2. Experimental setup

The diagram of our experimental setup is shown in Fig. 1. A DMD with 1024×768 micro-mirrors (Discovery 1100, Texas Instruments) driven by an interface board (ALP-1, ViALUX) was used to modulate the 632.8-nm laser beam, which was direction-adjusted by two mirrors (M1 and M2) and expanded by two lenses (L1 and L2). The DMD modulated light field was couple into the MMF with a tube lens TL1 and a 40X microscope objective OL1. Corresponding MMF outputs, magnified by a 20X microscope objective OL2 and the tube lens TL2, were recorded by the camera. In our setup, we set 2×2 micromirrors as a single macro pixel in the modulation to enhance the difference between the "ON" and the "OFF" pixels. We also used input patterns consisting of $N = 1296$ macro pixels and captured output patterns with $M = 9216$ pixels on camera. The number N is limited by the maximum number of modes supported in the MMF, as sufficient degrees of freedom are required to describe the change of input patterns. The number M is determined by the parameters of the MMF used in our experiment particularly the core diameter (50 μm in this case) and by the magnification ability of the objective lens used. In order to retrieve phase information successfully, $M/N \geq 2$ is needed according to the algorithm.

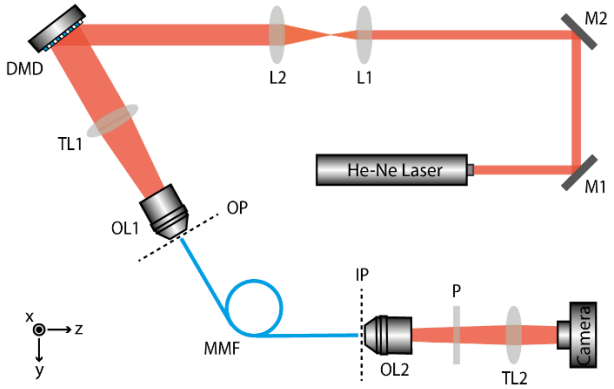

Fig. 1. Schematic experimental setup of reference-less MMF characterization. He-Ne Laser: 25-LHP-925-230, Melles Griot; M1, M2: Mirrors; L1, L2: Bi-Convex Lenses; DMD: Digital Mirror Device, Discovery 1100, Texas Instruments; TL1: Tube Lens, AC254-200-A-ML; TL2: Tube Lens, AC254-100-A-ML; OL1: 40X Objective Lens, Nikon; OL2: 20X Objective Lens, Olympus; MMF: Multimode Fiber, FG050UGA, Thorlabs; P: Polarizer, LPVISE100-A, Thorlabs; Camera: C1140-22CU, Hamamatsu; OP: Object Plane; IP: Image Plane.

In calibration, we fed the system with approximately P = 8000 input fields, which are random binary patterns with half pixels "ON" and half pixels "OFF". Alternatively, it might be most straightforward to light up one macro pixel each time and record the generated output (if with phase), which is actually a point spread function of the system and one column of its TM. However, we did not carry out in the latter way as the light diffracted by only one pixel is very weak, resulting in poor signal to noise ratio (SNR). With half pixels "ON", the response of a single macro pixel is measured $P/2$ times, improving SNR $\sqrt{P/2}$ times compared to the simple approach of turning on one macropixel at a time. Moreover, the DMD was operated at 250 Hz, limited by our camera as the DMD speed can be up to 8 kHz. With the latest models such as Discovery 4100 from Texas Instruments, the calibration can be done easily in one minute. Also note that system stability is critical and needs to be monitored during the whole experiment. We performed this by calculating correlation coefficients of outputs for the same input over time and the system was ensured 99% stable. The input and output data was processed with the prVBEM algorithm [16] after recording. In short, this algorithm infers one row of the output field phases and one row of the TM according to each other iteratively in a Bayesian way. The iteration is stopped if the changes of both are below the threshold (i.e., in stable states). The steady values are then returned as the most possible and estimated values for each item. This algorithm is also suitable for parallel computation since estimations of different TM rows are independent. In our implementation, high performance computing facilities were used to perform parallel calculation and it took 1 to 3 minutes to calculate one TM row with Intel Xeon Processor E5645 @ 2.4 GHz, depending on data size.

3. TM evaluation

In order to test the calculated TM, we compared the TM-predicted outputs with the actually recorded outputs by the camera for the same inputs in terms of the correlation coefficient, which is realized with the *corr2*/*corr* functions in MATLAB. The correlation coefficient was averaged over around 8000 input patterns and the relationship between data amount and calculated TM's prediction ability is described in Fig. 2. Here, P denotes the number of input patterns and N is the macro pixel count on DMD as mentioned before. It is found that more input fields for calibration could result in stronger prediction ability. In the view of Bayesian inference, the posterior probability distribution of the item being estimated will get updated and narrowed down when feeding the algorithm more and more data. Since the expectation value of the latest posterior probability is returned as the inferred value in the algorithm, the estimated value tends to deflect more from the true value if the data is not enough as the posterior is still relatively wide in this scenario, which could explain the undesirable TM

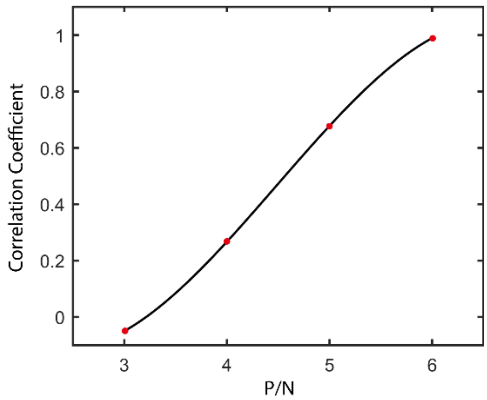

Fig. 2. Prediction performance expressed by correlation coefficient as a function of P/N. N is the count of macro pixels used on DMD while P denotes the number of measurements performed during calibration.

performance when P/N is insufficient. As the data is becoming bigger, the posterior would be sharp enough and the estimated value would therefore be very close to the true value, leading to clearly improved performance. For our setup, $P/N = 6$ is thought to be the threshold for a successful implementation as the corresponding prediction accuracy is around 99%, demonstrating high-quality TM estimation and precise prediction as offered by holography based methods. In the following parts, $P/N = 6$ was therefore used to ensure good performance and calculation was accelerated in a parallel way.

With TM, we are able to reconstruct the displayed DMD patterns based on recorded images on the camera. This represents imaging through the MMF in transmission mode. To demonstrate this, three pre-defined patterns ('LIV', '3.14' and a smiley face) were included intentionally in the input set. And the phases of corresponding outputs were recovered with the algorithm as done with other random input set. The inferred DMD patterns E_{OP} were calculated by solving the following linear equation:

$$TM \cdot E_{OP} = E_{IP} \tag{1}$$

where E_{OP} and E_{IP} stand for electric fields on the proximal fiber end and the distal fiber end, respectively. The E_{OP} may be calculated by using the inverse of TM. However, the TM is not a square matrix ($N \neq M$) in most cases, and has no a strict inverse matrix. The *pinv* function in MATLAB can be used to calculate the so-called pseudoinverse instead and it can work as a substitute of the strict inverse. Considering our TM shape (N is a few times of M), such replacement may cause additional noise. To solve the linear equation directly can avert this problem and this implementation is faster, especially for large TM. Note that to calculate pseudoinverse of large matrix can be very calculation-intensive. The inferred patterns are compared with the actual input patterns in Fig. 3. As shown, patterns can be observed distinctly through the MMF, demonstrating that the TM was estimated correctly and capable of undoing the information distortion caused by MMF effectively. Besides, the line width of three patterns was designed to be around 1.4 μm as an evaluation of system imaging resolution. Since the adjacent lines, as in Fig. 3(d) and Fig. 3(e), and small dots, as in Fig. 3(e) and Fig. 3(f), were separated well from the background and imaged clearly, the system imaging resolution is thought to be around 1.4 um, which is actually very close to the MMF's Abbe diffraction limit calculated as $\lambda/(2\mathrm{NA})$ = 1.44 μm. Therefore, our MMF has been demonstrated to be fully exploited and working with

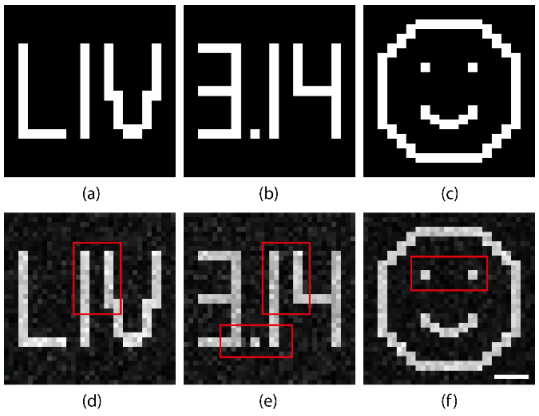

Fig. 3. MMF Imaging in transmission mode. (a) Original pattern of 'LIV'; (b) Original pattern of 3.14; (c) Original pattern of a smiley face; (d) Imaging result for the pattern in (a); (e) Imaging result for the pattern in (b); (e) Imaging result for the pattern in (c). Red boxes indicate the parts for resolution evaluation. Scale Bar: 5 um.

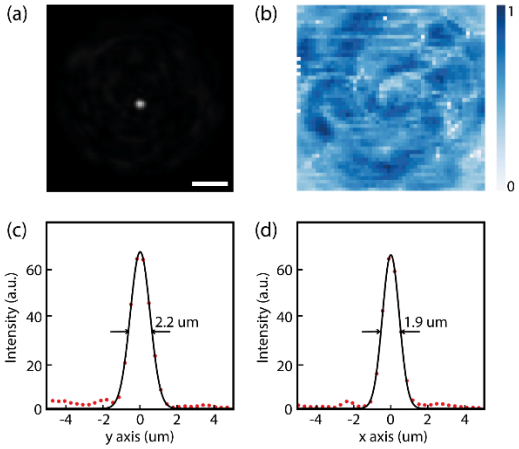

Fig. 4. Focus generation with the TM information. (a) A focus generated around fiber end center. Scale bar: 10 um; (b) Normalized EF distribution across a 50 by 50 grid within distal fiber end. Grid pitch: 0.58 um; (c) Intensity profile of the focus in (a) along y axis; (d) Intensity profile of the focus in (a) along x axis.

diffraction-limited resolution. To further improve imaging performance, one may want to utilize higher-NA MMF or to work with shorter-wavelength laser. In this part, DMD patterns worked as objects for the proof-of-concept study. Note that to do general imaging may involve matching the object/camera with the modulation device [7,8] since the TM depends on the modulator's specific position. To be precise, the optical distance between the modulator and the proximal fiber end should be equal to that between object/camera and the proximal fiber end. Additionally, when matching camera with modulator, it is also suggested that they have same pixel size and pitch and that transverse displacement is minimized.

Focusing through complex media has been an interesting topic over the recent years. In order to further evaluate our system, we utilized the information in the calculated TM to perform focus generation through the MMF. In detail, the complex conjugate of one TM row was chosen as a necessary input field for generating a focus on the distal fiber end. The position of the focus was controlled by choosing the corresponding row in the TM. To implement this complex input wave with DMD, we selectively turned on the macro pixels where the real part is positive. By doing so, we are able to create a clean focus through the MMF, such as the one around the fiber end center shown in Fig. 4(c) and Fig. 4(d) by fitting the data with a Gaussian function. The result indicates that the full width at half maximum (FWHM) of the focus in Fig. 4(a) is about 2.2 μm along the y-axis and 1.9 μm along the x-axis, We attribute the difference to the fact that the MMF is not an absolutely axisymmetric waveguide due to random fiber bending. The theoretical value of FWHM in our case is around 1.8 μm. And the degradation results from the difference between ideal input field and practical input field. Note that input fields are processed to be binary as DMD amplitude modulation is not continuous. Such field transformation will inevitably cause that doable input is actually different from the ideal one. Moreover, by choosing different TM rows, we scanned the focus across a 50 by 50 grid within fiber end and recorded the intensity enhancement factors (EFs), defined as the ratio of the focus peak value to the average value of output generated by a random input. The EF distribution is presented as a heatmap in Fig. 4(b). It is found that the maximum EF = 70 was obtained and the level of enhancement is obviously over the result achieved by genetic algorithm [16], thanks to fully exploiting spatial modes in the MMF and to accurate phase retrieval with the algorithm. Further improvement can be obtained by using more macro pixels on DMD and higher-NA fibers as done in [8]. It is also observed that the focus quality is not uniform over the fiber end. As mentioned, the modulation ability of DMD is limited by its binary feature and the actual input fields are more or less different from the ideal ones. Since the degree of such deflection

is case by case, it is reasonable that to generate a high-quality focus is difficult in specific positions, leading to an unbalanced EF distribution. To get a higher EF or a more balanced EF distribution, one may want to utilize more macro pixels on DMD or to use SLM instead (slower however) as both approaches will bring stronger modulation ability and control the input field more precisely.

4. TM properties

To the best of our knowledge, most of the work in this area used transmission matrix to generate specific patterns or to realize imaging. However, as a description of the corresponding system, TM's other information has not been studied extensively. In this section, we are to analyze TM mathematically and to extract information on fiber mode count and eigen channels for best energy delivery.

Fibers are not straight and deformation-free in most practical applications. The bending or twist of multimode fibers would impact mode properties such as mode propagation constant, mode transmittance as well as mode count in a specific fiber, leading to potential problems when utilizing multimode fibers to deliver information. Compared to ideal fibers, it is much harder to confirm the mode properties of a practical fiber with deformations to some degree. For ideal multimode fibers, one can easily estimate the mode count N_m by

$$N_m \approx 0.5 \times V^2 \tag{2}$$

where V stands for the normalised frequency of the multimode fiber. Equation (1) is obtained by solving Helmholtz function for step-index fibers and it is assumed V is large enough. Further, the normalized frequency can be calculated by

$$V = 2\pi a \cdot NA / \lambda \tag{3}$$

where a denotes fiber core radius, NA stands for its numerical aperture and λ is laser wavelength. When dealing with fibers with deformations, one can hardly solve the wave equations due to the asymmetry of fibers, complex boundary conditions and unknown deformation situations. Therefore, it is not easy to achieve the mode properties of randomly deformed multimode fibers. In the previous section, we demonstrated that transmission matrix of a multimode fiber imaging system can be achieved in a reference-less setup. This transmission matrix is able to describe how light field is changing through the whole system by relating independent modes on input plane with those on output plane. Here, we further demonstrated that it is practical to achieve the actual mode count in a multimode fiber by calculating the rank of its transmission matrix.

In the viewpoint of mathematics, the elements in transmission matrix are coefficients of linear equations relating input and output pixels. Therefore the rank of the matrix indicates the count of independent equations, which is also the number of degrees of freedom in the imaging system. Note that the input light fields need to couple into fiber modes to propagate in the multimode fiber and that the number of the spatial modes is the count of degrees of freedom of the system. Therefore we can deduce that the rank of transmission matrix [17] is actually the number of modes travelling in the multimode fiber. Since we can record transmission matrix in the experiment, it offers a practical method to achieve a number of fiber modes regardless of the specific states of deformations and abnormal solutions of wave equations.

To record the transmission matrix of a specific multimode fiber, we used the experimental setup introduced in the last section. Please refer to Fig. 1 for detailed information. In short, a number of random input patterns are displayed on the DMD and are delivered into the fiber proximal end. The corresponding output images on fiber distal end are captured by the camera directly without interference. The prVBEM algorithm is then utilized to infer the phase

information in output images and to calculate elements in transmission matrix. With the TM, one can easily obtain its singular values by singular value decomposition:

$$TM = U \cdot S \cdot V^{*} \tag{4}$$

Here, U and V are unitary matrices while S is a diagonal matrix with non-negative real numbers on diagonal, which are singular values of TM. In theory, the rank of the TM is the count of positive singular values.

In Fig. 5, we presented the singular value distribution of the TM of a multimode fiber. It is clear that the singular value drops obviously with the increasing of mode index. Since the squared singular value indicates mode transmittance, our observation is in line with the fact that higher-order modes experience larger loss. Also note that all the singular values are positive strictly in this TM, indicating the rank of TM is 1296. However, considering the noise level in the system, we used 0.01 as our threshold and achieved effective rank as 840. This

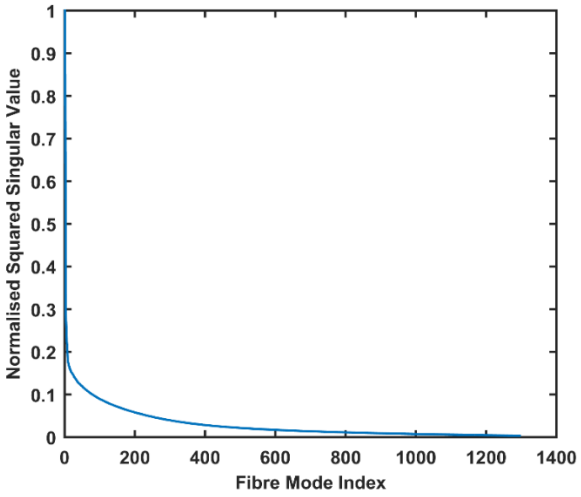

Fig. 5. Distribution of singular values of the TM.

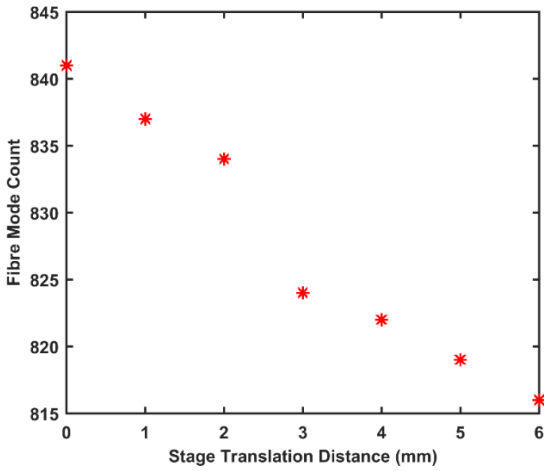

Fig. 6. Change of fibre mode count over additional stage translation.

number is close to 755, half of the estimation of from Equation (2). The reason why half estimation is used here is that polarizer is utilized in our experimental system. Therefore fiber modes in one polarization direction are filtered out. Considering this, we can still see the difference. And this is due to two reasons. First, Equation (2) is more accurate for large normalized frequency while the one for this multimode fiber is around 50. Second, Equation (5-1) is for ideal straight fiber while the real fiber is with imperfect index distribution as well as random bending or twisting. Moreover, it is reasonable that the number of modes supported in the multimode fiber is up to its geometry, which cannot be explained by Equation (5-1). Here, we further translated the additional fiber stage to observe the change of transmission matrix rank. As presented in Fig. 6, one can see fewer fiber modes are supported in the fiber if more translation is introduced. In our setup, more translation leads to more severe bending. According to fiber theory, energy is more likely to couple to cladding modes or radiation modes in this case. Therefore it can explain why we see the decreasing of fiber mode count. The energy coupling efficiency is up to input field distribution as well as fiber mode distributions.

Normally, more overlapping between input field and mode field will result in better coupling efficiency. Also, different modes experience various transmission loss and this is also related to specific fiber geometry. Therefore the energy transport efficiency is different for distinct input patterns. In Ref. [18], Choi's group studied eigenchannels in scattering medium to maximize energy delivery efficiency. To the best of our knowledge, similar work has not been done for multimode fibers. Here, we measured the transmission matrix of multimode fibers and demonstrated corresponding eigenchannels to effectively enhance energy transport. The experimental setup is the same as in Fig 1. And we are able to construct full transmission matrix without interference thanks to the help of prVBEM algorithm as demonstrated. Similarly, we also need to perform singular value decomposition

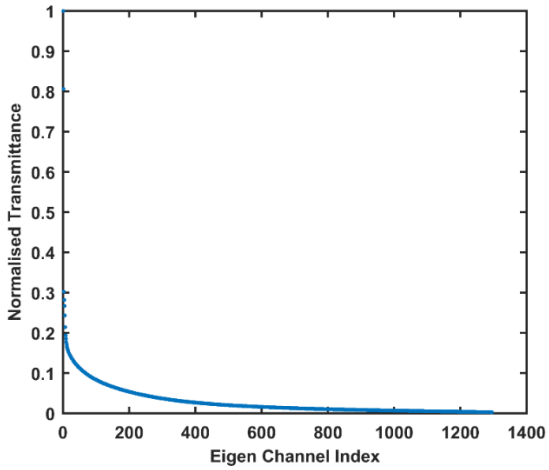

Fig. 7. Normalised transmittance of eigen channels.

for the transmission matrix according to Equation (4). Previously, the effective rank of matrix S is used to determine the mode count in a specific fiber. Here, we further demonstrated that the column vectors in matrix V are actually eigenchannels in the transmission matrix and the first one of them corresponds to the input patterns with maximum energy delivery efficiency. With a TM, we can first study the energy transport for each eigen channel theoretically. In order to do this, we virtually injected column vectors of matrix V into the fiber and obtained corresponding outputs with the help of TM. The normalized energy delivery efficiency is shown Fig. 7 and one can clearly see the descending trend, indicating the first column vector is optimal for energy transport. Besides, the normalized energy delivery efficiency values are exactly the normalized squared singular values, indicating the physical meaning of the singular

values of transmission matrix. Note that we measured output images for random input patterns in order to construct TM. Here, we used these input and output data to calculate the energy transport efficiency for random input patterns. In addition, we implemented the best eigen channel and recorded the corresponding output. The energy

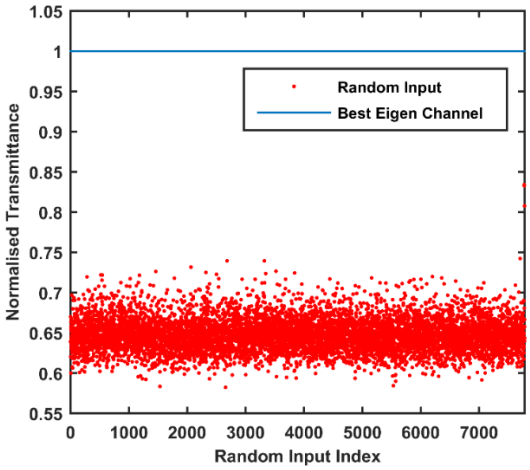

Fig. 8. Normalised transmittance for random input patterns.

delivery efficiency for random patterns is normalized to that of best eigen channel and the results are presented in Fig. 8. In this experiment, we can observe that the energy transport efficiency for the eigen channel is obviously higher than that of random patterns. Specifically, one can expect over 1.5 times enhancement. However, this value is still certainly away from theoretical enhancement which is around 8 times in our case. The primary reason for this observation is that it is only possible to realize binary amplitude modulation with the DMD.

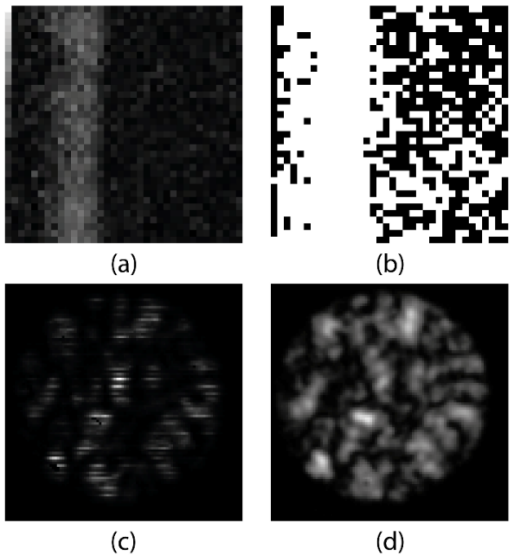

Fig. 9. Comparison of the ideal and practical eigenchannels. (a) Ideal input amplitude; (b) Practical input amplitude; (c) Theoretical output pattern; (d) Realistic output pattern.

The practical eigen channel and perfect eigen channel are compared in Fig. 9 where we also present their corresponding output patterns. As shown, due to the difference between the realistic pattern and the ideal pattern, the outputs are clearly distinct, leading to lower energy delivery efficiency. This drawback significantly limits our ability to generate accurate patterns on the fiber proximal end as mentioned in the last chapter. But the energy transport efficiency was apparently improved even with the imperfect input patterns, demonstrating the existence of eigenchannels. Also, one can expect to see a great improvement if using phase modulator such as SLM.

5. Conclusions

In summary, distinct from previous methods, it has been demonstrated that full transmission matrix of an MMF is achievable in a reference-less setup and with phase retrieval techniques. Such configuration leads to not only a simplified system but also better system stability. The TM is calculated by the phase retrieval algorithm, which can be accelerated by distributed calculation. The generated TM has also been examined to have strong prediction ability, to be able to perform diffraction-limited imaging and to be capable of concentrating light into a clean focus. Furthermore, it has been demonstrated that information on mode count and eigenchannels is available from TM by singular value decomposition. It is believed that the proposed setup improves the current approaches and opens a new way for MMF characterization. As a fast and robust implementation, it can also be a promising candidate for MMF focusing and endoscopic imaging.

Funding

This work was supported by the Engineering and Physical Sciences Research Council [grant number EP/L022559/1]; the Royal Society [grant numbers RG130230 and IE161214].

Acknowledgements

Liang Deng would like to thank University of Liverpool for financial support. This research utilized MidPlus computational facilities in Queen Mary University of London.